ORNL/SPR-2019/1113

Execution of Targeted Experiments to Inform BISON for ATF Materials: An Advanced Approach to Tube Burst Testing

Nuclear Technology Research and Development

Prepared for
US Department of Energy
Advanced Fuels Campaign
M. Gussev,
M. Howell,
K. Terrani,
A. Nelson
Oak Ridge National Laboratory
February 8, 2019
M4FT-19OR020201065

SUMMARY

This report describes a new, advanced experimental approach for testing tube specimens loaded by internal pressure. The approach allows conventional tube burst testing to be performed and employs digital image recording and analysis for conducting noncontact optic strain measurements. Section 1 provides a brief introduction and motivation for the project. Section 2 describes the selected approach and provides technical details regarding the modified experimental tube burst system: a commercial infrared furnace redesigned to support this work by adding two 50-mm- diameter optic ports to make the specimen visible during the burst tests, and a digital camera used to record specimen images, lens, and optic filters.

Section 3 briefly analyzes a typical burst test and the digital image correlation dataset, recorded during the experiment, and discusses the experiment outcome, including local strains along the tube specimen. Additionally, Section 3 focuses on the issues influencing the in situ strain measurement accuracy and final results and suggests changes in the experimental scheme to improve data quality and reliability. The conclusion summarizes the work performed to date and discusses the possible future activity.

CONTENTS

FIGURES

ACRONYMS

DIC	digital image correlation
fps	frames per second
LOCA	loss-of-coolant accident
LWR	light-water reactor
MPix	Megapixel (~1 million pixels); parameter describing image quality and resolution
ORNL	Oak Ridge National Laboratory
TC	thermocouple

ACKNOWLEDGMENTS

This work was supported by the Advanced Fuels Campaign of the US Department of Energy Office of Nuclear Energy. The authors would like to thank Dr. S. Raiman (ORNL) and Dr. K.G. Field (ORNL) for fruitful comments and reviewing the present report and L. Varma (ORNL) for valuable help with document preparation.

AN ADVANCED EXPERIMENTAL APPROACH FOR TUBE BURST TESTING

1. INTRODUCTION

1.1 Motivation

Under both normal and accident conditions, the nuclear fuel cladding is the most critical core structure in fission reactors because it is subjected to extreme conditions and must function as the first safety barrier [1–3]. A fuel cladding material is selected considering a variety of performance metrics such as neutron absorption cross-section, mechanical strength and ductility, irradiation and thermal creep resistance, resistance to embrittlement, thermal properties, corrosion, and chemical compatibility [1]. Cladding behavior and performance governs the cooling efficiency of flow channels and the process of fission product release; thus, during a loss-of-coolant accident (LOCA) [3], the most important property of fuel cladding might be the resistance of the cladding material to plastic deformation and burst at elevated LOCA-relevant temperatures. Therefore, the key performance metric for demonstrating accident tolerance should include the deformation-to-burst behavior of tubular specimens under LOCA condition.

The importance of this aspect of cladding behavior has prompted efforts to model anticipated evolutions in material properties experienced during service upon tube burst (e.g., irradiation damage, hydrogen pickup). One common tool is BISON, a finite element-based fuel performance code that has been developed and advanced by the Office of Nuclear Energy research under multiple programs. BISON—and proprietary fuel performance codes such as those used by nuclear fuel vendors—use numerical methods to predict fuel behavior as a function of material properties. It is therefore possible for researchers to implement property correlations and assess the impact of individual parameters on system performance. For example, the effect of fission gas release on cladding stress during fuel service can be isolated and studied to assess proposed improvements in fuel design. This is a powerful tool not only to guide research but also to probe the sensitivity of important licensure criteria for a range of material properties.

The ongoing challenge involves the production of experimental datasets that can serve as validation tools for BISON and other predictive codes. The complexity of nuclear fuel element evolution during service is well appreciated. Also, irradiation leads to radioactivity, greatly complicating the use of many material characterization methods. Even basic microstructural characterization of irradiated fuel and cladding comes at the significant expense and with great limitations when compared to what is possible for unirradiated material. Researchers who use state-of-the-art computational tools to predict fuel performance are, therefore, left without applicable benchmarks, thus limiting confidence and increasing the potential for skepticism. Recent research focused on the effect of fission gas on cladding burst provides an illustrative example. Figure 1 highlights BISON predictions of clad ballooning at burst as a function of two fuel types that exhibit a range of fission gas release behaviors. This simulation was aimed at comparing the influence of fission gas release as affected by doping of the fuel.

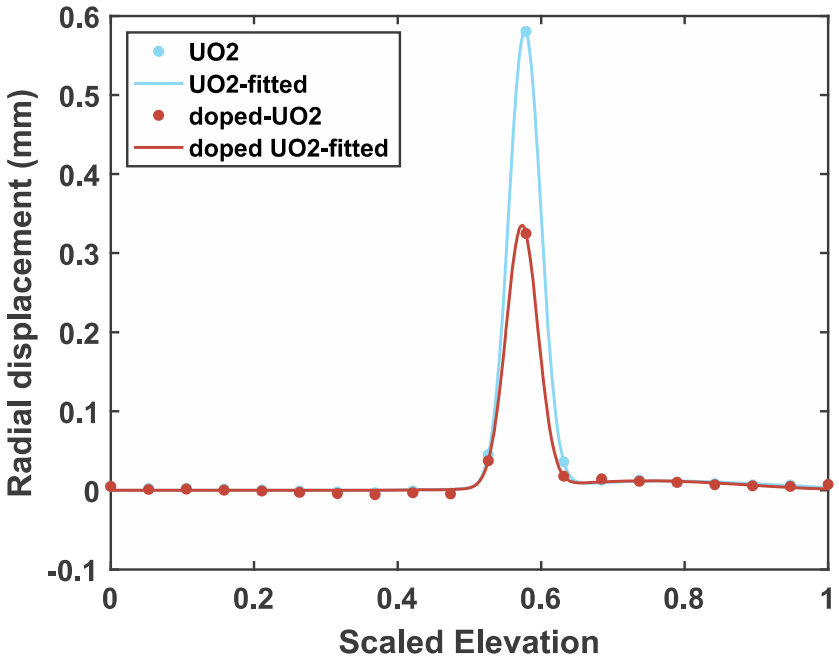

Figure 1. Radial displacement of the cladding at burst for reference and doped UO_2 predicted using BISON [4].

In contrast to the predicted behavior, radial displacements as measured experientially exhibit more complex behaviors. Figure 2 highlights diametrical measurements made following an experimental investigation of the same phenomena (i.e., large-break LOCA) plotted in Figure 1. The specifics of the available experimental investigation [5] do not match those simulated—another challenge to benchmarking—and thus do not merit a detailed comparison, but Figure 1 and Figure 2 clearly exhibits multiple asymmetric displacement peaks. This indicates more complex behavior than can be captured by the BISON material models or cladding failure criterion as presently employed.

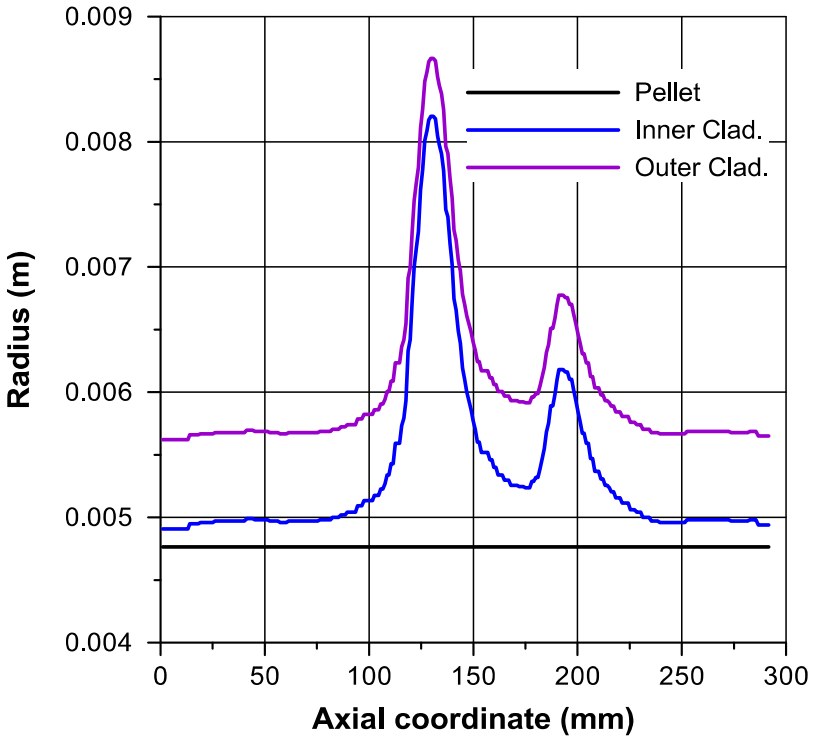

Figure 2. Experimentally determined radial displacement profile of zirconium–UO_2 ramped in steam to simulate the environment simulated in Figure 1 [4].

The most efficient solution to improving the ability of modelers to both inform and benchmark their simulation capabilities as embraced by the Advanced Fuels Campaign is a ‘separate effects” approach. The premise of this philosophy is the execution of experimental campaigns focused on exercising a single independent variable to produce datasets that are of high utility to the modeling community. In the case of cladding burst, the most logical initial step in this effort is the removal of irradiation, oxidation, and fission gas release to provide high-fidelity datasets that describe strain evolution as a function of the stress state. This experimental approach has generally used burst testing.

Traditionally, tube burst testing using high-pressure gas was performed to measure the burst temperature as a function of the internal pressure and to assess the performance of new and irradiated cladding materials [6]. However, this kind of test, Figure 3, has a very limited outcome, yielding only one point in the temperature-pressure coordinates. Therefore, to fully simulate cladding behavior during severe accidents, additional information ideally should be gathered regarding the material behavior to provide a full picture of stress and strain evolution as a function of temperature and/or internal pressure and stress state. To reach this goal, an advanced, more efficient testing approach (or approaches) must be developed to provide more information compared to a conventional tube burst scheme. This research aims to offer and evaluate a new testing method for investigating cladding behavior that is directly applicable to the benchmarking of modern modeling and simulation approaches.

1.2 Path Forward

Over the last decade, researchers have developed a range of experimental approaches that include specimen observation and in-situ measurements as part of the experiment design [7–9]. Regarding the cladding tube specimen, in-situ analysis allows for creep rate evaluation and estimation of true stress in

the wall. All these in-situ methods are based on specimen recording in the visible, infrared, or ultraviolet light range [7,8,10]. Currently, high-performance video cameras have become affordable for dimensional measurements, providing data with high resolution and high transfer rate. Recent advantages in the digital image correlation (DIC) algorithms allowed for strain and displacement calculations with high accuracy and precision. Thus, employing specimen optic observation, image recording, and DIC analysis [8,11,12] would be the next logical step to further develop the capabilities of tube burst tests under LOCA-relevant conditions.

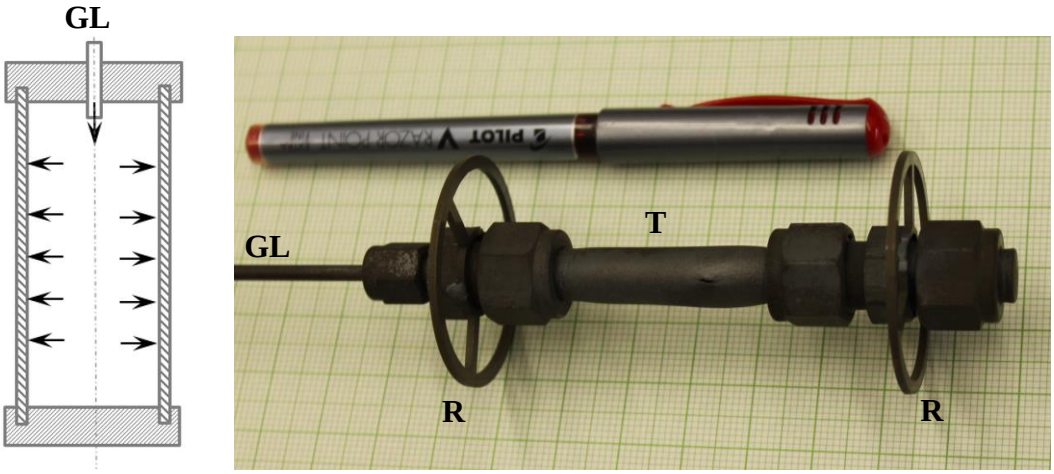

Figure 3. A schematic of the tube specimen, loaded by internal pressure (left) via gas line (GL) and the tube specimen (T) after burst testing (right); the gas line pipe is visible. The centering rings (R) stabilize the specimen in the middle of the quartz tube.

2. ADVANCED TUBE BURST TESTING APPROACH

2.1 General Scheme

During conventional LOCA-relevant tube burst testing, the tube specimen (Figure 4), is loaded by internal pressure. The specimen is located inside a quartz tube in a water vapor atmosphere to investigate the material's interaction with steam. Image recording during a test can be used to view and evaluate changes, as long as the camera and lens are suitable for the given working distance and object size [12]. Optic filters are also important to optimize light conditions and intensity and to minimize unnecessary spectra components, as discussed in [7,8].

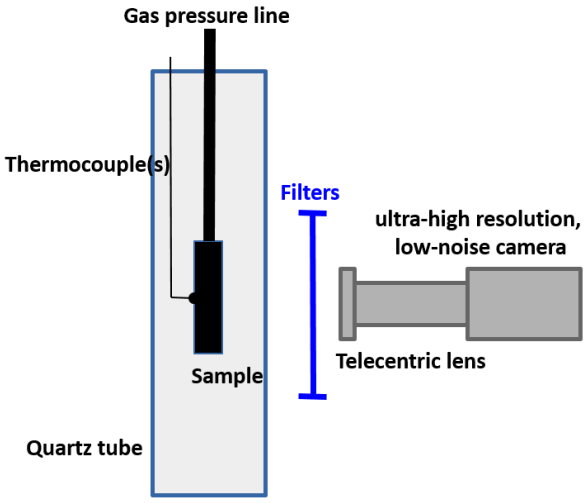

Figure 4. Scheme of the improved tube burst test.

The project reported here employed an Allied Vision GT6600 camera with ~24 MPix matrix (6576 × 4384 pixels); the camera supports GigE interface with a dataflow rate up to 120 Mb/s, which provides a frame rate of 4 fps. This frame rate is sufficient for the present project, at the 5°C/s heating rate. Later stages of the experiment, when ballooning and plastic deformation occur, may need faster imaging. This possibility will be considered in the future.

To provide object visibility, a commercial infrared furnace (Figure 5) was modified by a vendor. The furnace uses four infrared heaters, located in the focus of parabolic mirrors, to heat the object. The mirrors reflect and redistribute the emitted light to provide uniform energy flow inside the furnace. Water-filled channels in the furnace body preserve the mirrors and the furnace exterior from overheating and oxidation.

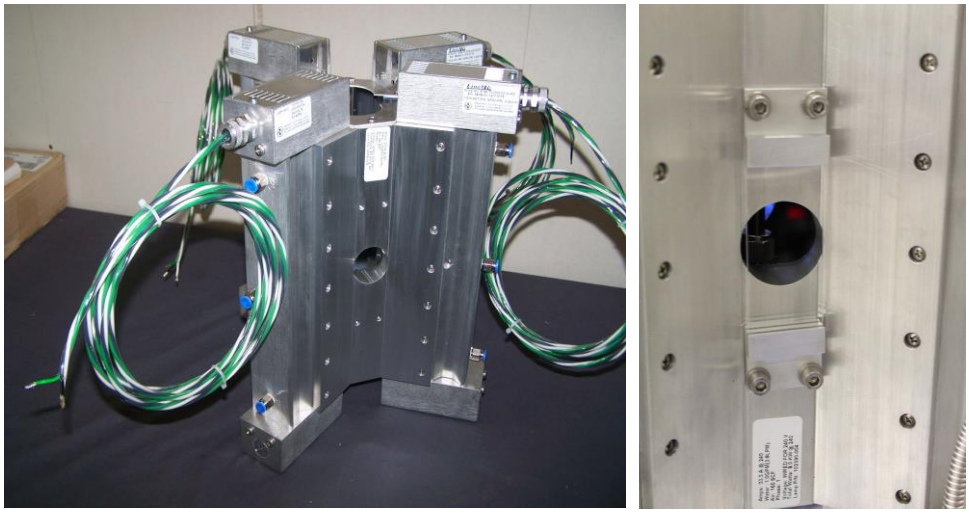

Figure 5. Modified infrared furnace (left). The custom design included two optic ports (right) enclosed by optic-quality quartz glass to reduce heat losses.

For this project, two optic ports were included in the design, and the port size was 50 mm (2 in.) (Figure 5). Port locations (on the front and back sides) were selected to minimize the impact on the energy flow and distribution inside the furnace. Larger port dimensions may be considered in the future, but this change will require a very careful analysis of heat losses and temperature fields inside the furnace and at the sample surface.

The quartz tube was also changed; the round tube was replaced by custom design, with a flat window added on one side (Figure 6). The flat window was made of an optic-quality thin quartz plate to provide specimen visibility and minimize optical distortions. Because quartz is transparent in the infrared part of the spectra, it was believed that the window and tube geometry change had minimal impact on the tube specimen temperature field.

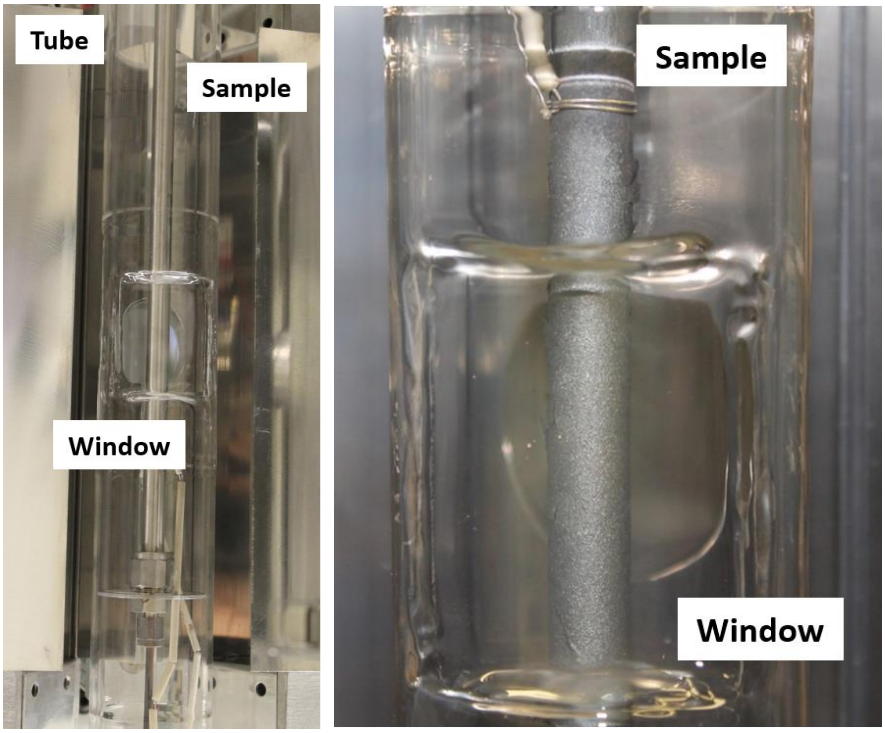

Figure 6. Design of the internal quartz tube with a standard 1-feet tube specimen. The window was added to provide specimen visibility and eliminate distortions. Note, the standard 1-feet tube specimen is shown in the images.

Preliminary tests employed a conventional long-distance lens with variable working distance. The calibration grid was employed in trial runs to evaluate the contribution of turbulence and convention on image stability and measurement accuracy. Increased working distance (up to 1 m) prevented lens and camera heating by thermal irradiation. However, trial runs demonstrated that the specimen shifts position slightly inside the quartz tube. The analysis showed the shifts were caused by deformation of the specimen and holder due to temperature gradients. Instead of their small amplitude (~2–3 mm), these shifts resulted in blurry images. In this project, shifts to the left and right were not critical, but shifts toward and away from the camera led to the appearance of fictional strains in the recorded images. Additionally, conventional lenses prevented the research team from keeping the whole object in focus because only one area could be focused at one time (e.g., specimen edge or specimen front surface) (Figure 7).

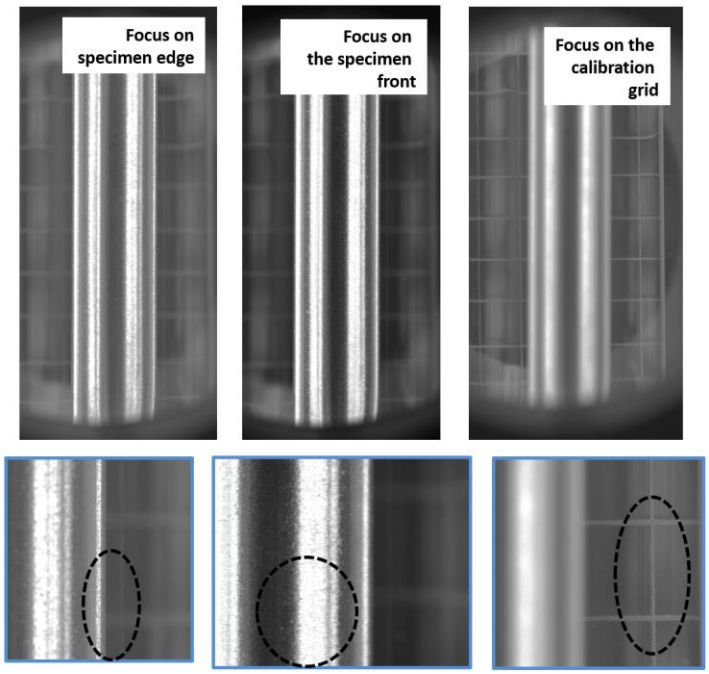

Figure 7. Images recorded using conventional lens; the focus was on the edges (left images), specimen front side (middle images) or calibration grid (right images).

A telecentric lens was employed to mitigate specimen shift. As an advanced class of optic devices, telecentric lenses have a much higher depth of focus than conventional lenses, producing images in which an entire object is in focus (Figure 8). Additionally, because these lenses use a parallel light beam, shifts toward and away from the camera do not produce fictional strains because object size remains the same. However, with a telecentric lens, the working distance cannot vary and must be selected at the system design stage.

For the selected telecentric lens (model TCCR4M080-F, Opto Engineering Inc., www.opto-e.com), the focus depth was ~25 mm, and the resolution at a working distance (~30 cm) was estimated to be 25μm/pixel. Using the lens, the whole tube specimen was focused (Figure 8). Additionally, this lens has a special optomechanical design, minimizing lens length, weight, and occupied space.

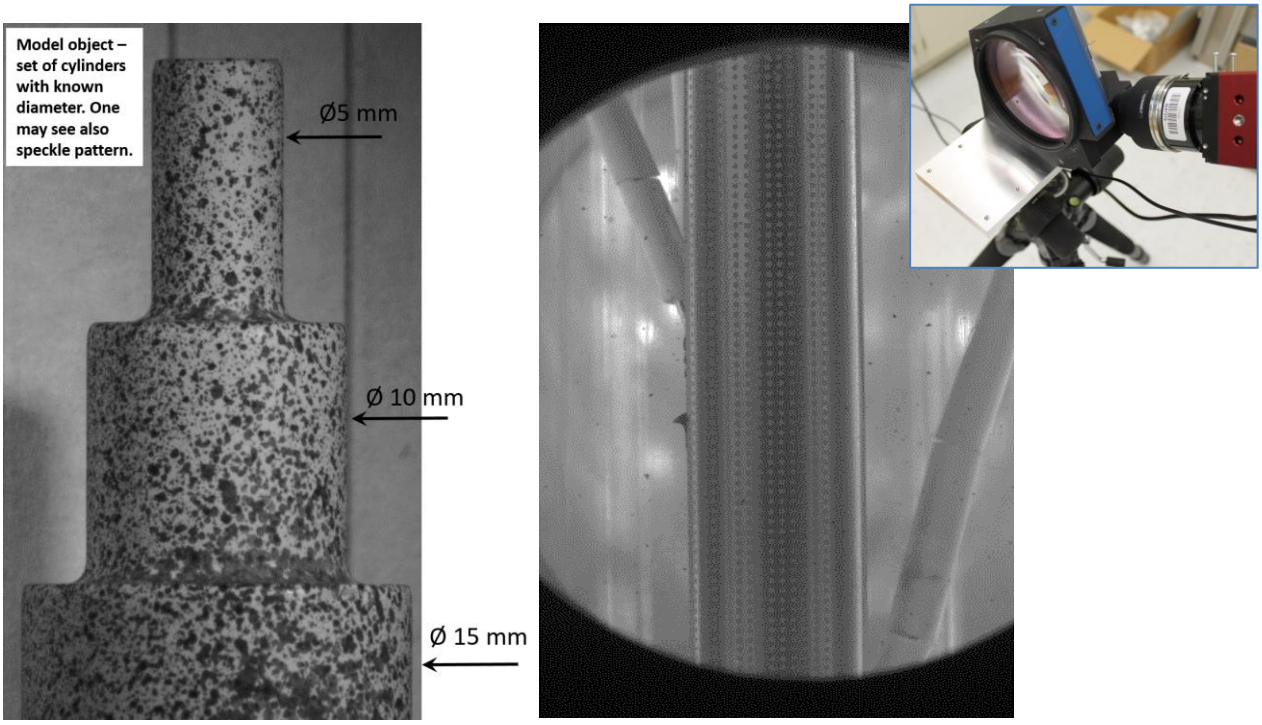

Figure 8. Image of the model object (left) and tube specimen (right) recorded using the telecentric lens. Inset at the right shows the selected telecentric lens.

Optic filters are a mandatory part of most high-temperature DIC systems [7,8]. The furnace employs infrared heaters, and maximum energy emission is in the infrared part of spectra. Nevertheless, the visible light intensity is high enough and may completely flood the camera sensor. A 460 nm band pass filter was employed, removing most (>99%) of the spectra and transmitting only a limited wavelength range (~450–470 nm, which corresponds to the blue light). The camera sensor has better sensitivity in this range. Additionally, the variable neutral density filter was added to the design.

2.2 Temperature Measurements

The system controller design allows for up to four thermocouples (TCs) to run simultaneously during the test. The routine experiment scheme employs two TCs:

- A control TC is located in the specimen middle opposite the observation window.
- A second TC (i.e., over-temperature control TC) is employed for safety reasons to prevent overheating if the first TC fails during testing. This TC is usually located at the back of the specimen.

Calibration experiments can use all four TCs located along the axis to measure the axial temperature distribution or along the specimen center to evaluate the radial temperature variation (Figure 9). This capability may be especially important at the results analysis stage; temperature gradients during the tube burst test are rarely discussed in the literature, whereas this factor may be critical for short specimens.

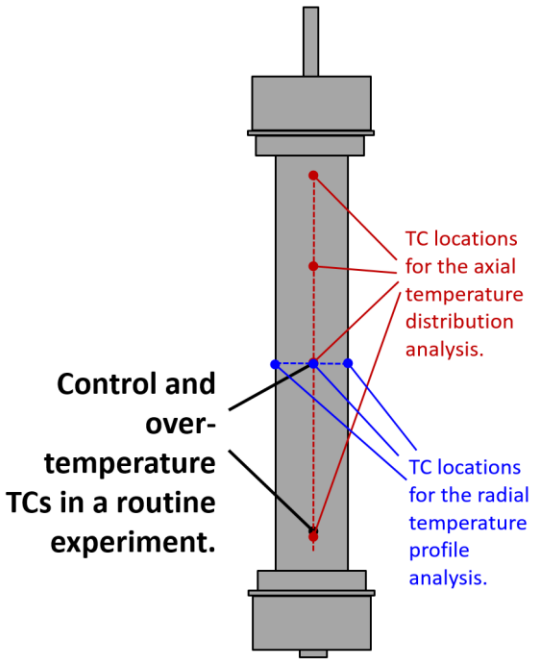

Figure 9. Thermocouple locations for temperature measurements during the test.

In the future, the number of TCs may be changed if necessary. To investigate temperature gradients in more detail, a thermal vision camera may be employed in conjunction with conventional ones. Semitransparent mirrors may be used to share the optic stream between the thermal vision system and optic camera.

2.3 Laser Engraving for Creating DIC Patterns

Digital image correlation (DIC) analysis requires some features (often termed "speckles" [11,12]) to present in the images; using special algorithms, these features may be precisely tracked allowing for displacement and strain calculations. However, the conventional approach to creating the DIC pattern (i.e., white and black paints) is not acceptable for the tube burst test. Paint layer will influence material oxidation kinetics and interaction with steam.

An alternative method could involve using natural marks (e.g., weak scratches, tool marks) that are always present at the specimen surface. Unfortunately, trial runs demonstrated that natural marks are usually weak and may not serve as a reliable DIC pattern; they quickly disappear during the test, leading to the lost of tracking. Patterns with natural marks, as a rule, have very low contrast, preventing the use of common DIC algorithms. Further development of DIC tools and robust image analysis algorithms may expand tube burst testing capabilities; however, currently, tubes with "natural marks," without an artificial high-contrast pattern, are insufficient for DIC-accompanied burst testing.

After several trials, laser engraving was found to be an effective method to create DIC patterns. The laser transfers any gray-level image on the tube specimen surface, and the pattern survives at least early stages of the test, up to 1100–1200°C. The depth, shape, size, and contrast of the marks may vary widely and likely may be adapted to most materials of interest. Figure 10 shows one of the trial patterns applied to the FeCrAl (iron–chromium–aluminum) and Zr-4 (Zircaloy-4) tube specimens. This regular pattern has high contrast and good visibility and may be easily modified (e.g., creating a nonregular or quasi-random grid), if necessary.

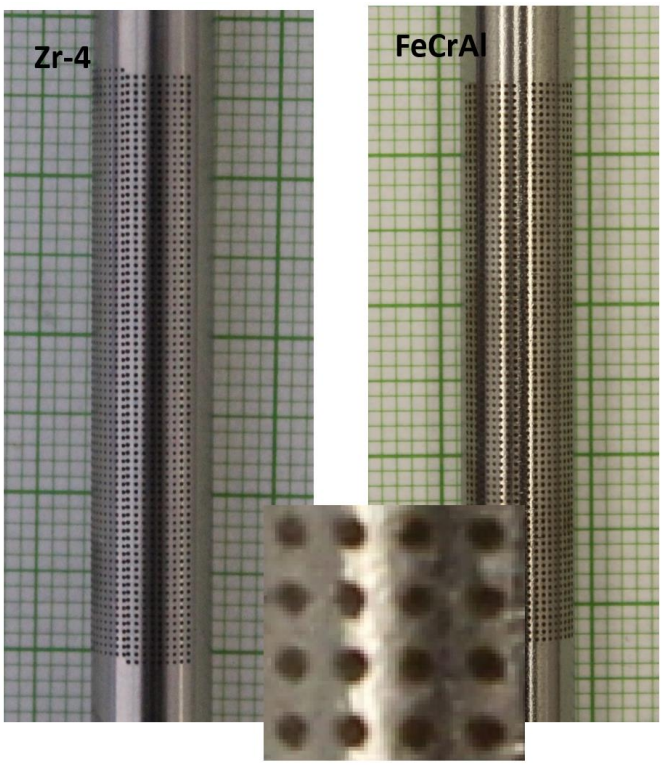

Figure 10. DIC patterns created by laser engraving.

3. ANALYSIS OF TRIAL TUBE BURST TEST

3.1 The sequence of Events during Typical Tube Burst Testing

Figure 11 demonstrates the chronology (i.e., the sequence of events) for a typical burst test. The test plan includes specimen preheating at 300°C; after this temperature is reached, the system remains at that temperature for 5 min. During this time, the quartz tube filled with water vapor reaches an equilibrium state, and the specimen surface experiences initial weak oxidation. This temperature—300°C—is close to the normal operation temperature of most light-water reactors.

After a 5-minute pause, the burst test began; the temperature increased at a rate of 5°C/s, which is a standard ramp rate for most LOCA tests. At some point, due to the internal pressure applied, the tube specimen experiences burst. The burst event is visible as a fast (but very short) drop in temperature. Gas expansion decreased specimen temperature, and the furnace control system compensated this temperature drop by adjusting the heater power.

After the temperature reached ~1150°C, there was a second hold step; during the 5-min span, the specimen experienced additional oxidation from water vapor. After that, cold water filled the quartz tube, causing a fast drop in temperature and material quenching.

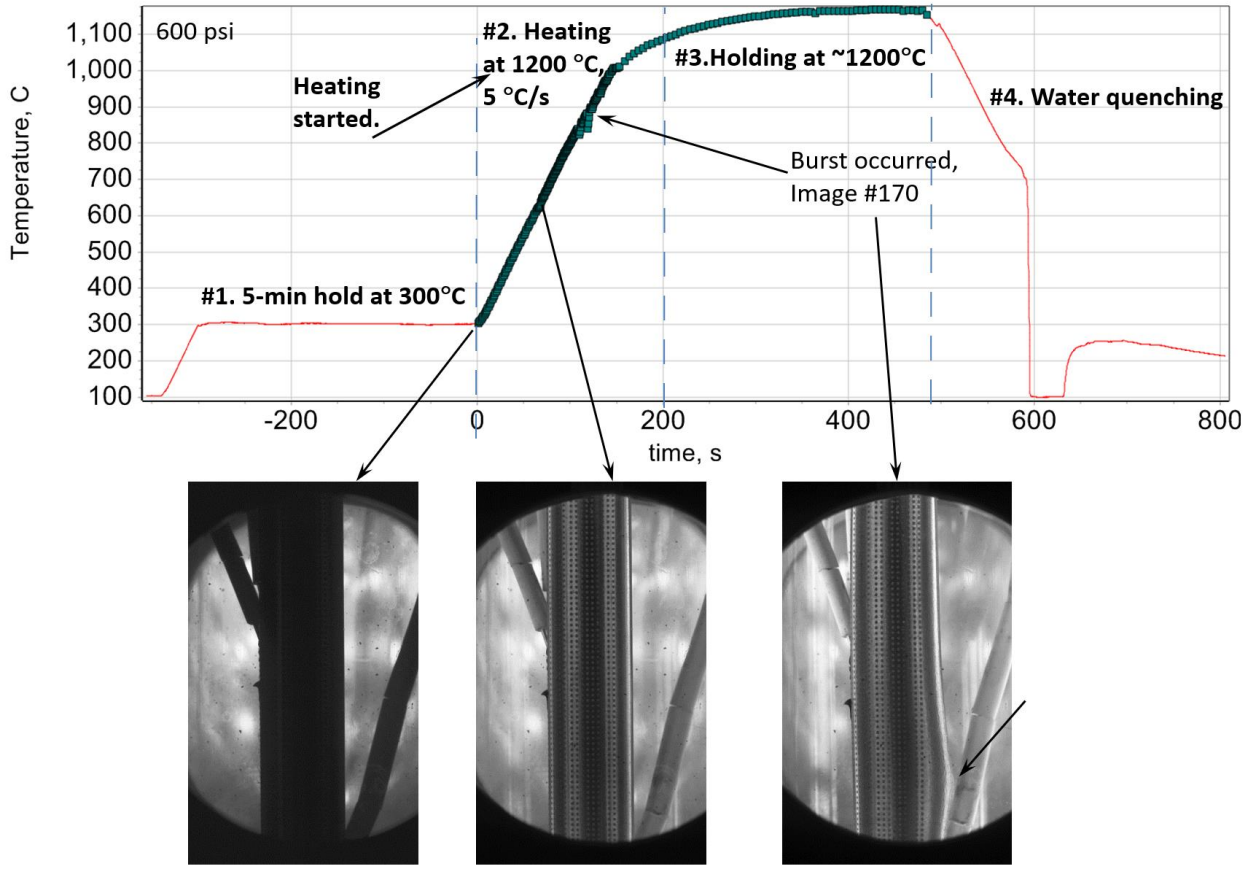

Figure 11. Events during typical tube burst test and images recorded by the digital camera.

Strong variations in the temperature (from room temperature to ~1200°C) lead to significant changes in the intensity of the power. Light intensity changes of a few orders of magnitude were often flooding the digital camera sensor. The camera setting allowed for some changes in the sensitivity, brightness, and

contrast, but these were not sufficient to handle the light intensity jumps. External variable filters may help, but in reality, researchers need to target some range of temperatures (e.g., 500°C to 1000°C) and optimize filter and camera setting for the best specimen visibility and image quality inside this range.

For instance, the specimen image is too dark at 300°C (Figure 11, left), but at ~550–600°C the specimen and DIC pattern are sufficiently visible.

Figure 12 shows a set of images recorded at different temperatures. For the temperature range of ~400–900°C, the specimen edges are well contrasted and easy to track. In the figure, water drops are visible at 403°C. Arrows at 549°C show bright lines (i.e., reflections from the heaters). The arrow at 701°C points to dust/oxide particles. At the beginning of the burst test (403°C), water drops form, instead of elevated temperatures in the sample, because the quartz tube is still sufficiently cold due to optic transparency, and water vapor condensate appears, creating optic noise in the image. Water drops move along the internal quartz tube surface, creating "noisy," noninformative objects in the images. This kind of "noise" is a negative factor, complicating the automatic DIC analysis. Most of conventional DIC algorithms and software cannot deal with such mobile, periodically appearing objects, which disturb the view field.

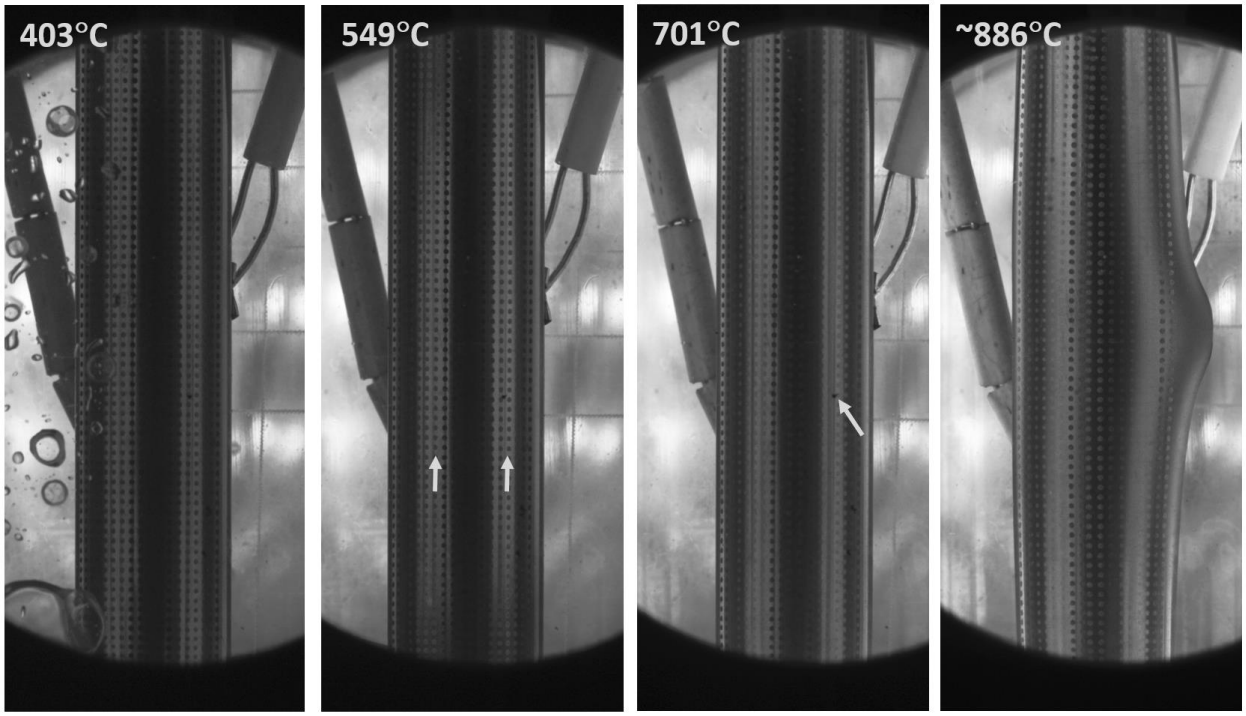

Figure 12. Examples of images recorded at different temperatures during the test.

The water drops disappear at ~500–550°C; however, continuous specimen oxidation and vapor circulation inside the tube combine to produce particles. These particles, appearing at the specimen or tube surface, also create some visual noise, reducing accuracy during DIC analysis.

3.2 Strain Measurement Example

Using the installation described above, several trial tests were performed with cladding tube specimens. The focus was made on testing FeCrAl alloy tubes, as this is a promising material family of high current and potential interest. This section does not aim to provide a comprehensive description of the results, but instead to demonstrate and highlight the capabilities and potential outcome of the approach.

Figure 13 shows the hoop strains at different locations of the tube specimen during tube burst testing. The hoop strain values were calculated using 2-point virtual digital gauges (#1–#3) placed at a range of locations. The measurements started at ~550°C, when specimen visibility and contrast, as well as light conditions, became sufficient (Figure 11 and Figure 12). As the temperature increased, the hoop strains increased linearly, most likely due to creep and temperature-induced changes in the Young modulus. At ~780°C, plastic strains appeared in the data as an obvious deviation from the close-to-linear relationship. As the temperature increased, plastic strains increased for all tracked locations, with gauge #1 demonstrating the largest strain level. The burst was observed at ~870–880°C. During the burst event, the temperature reading from the attached TCs revealed some disturbance (i.e., fast decrease and increase). The sample shifted in the field of view, and gauge #1 lost track due to the bulge formation.

After the burst, strain did not change, and the changes in gauge readings were caused by image disturbance and air turbulence (gauge #2) or surface oxidation, pattern change, and loss of tracking (gauge #3 in Figure 13).

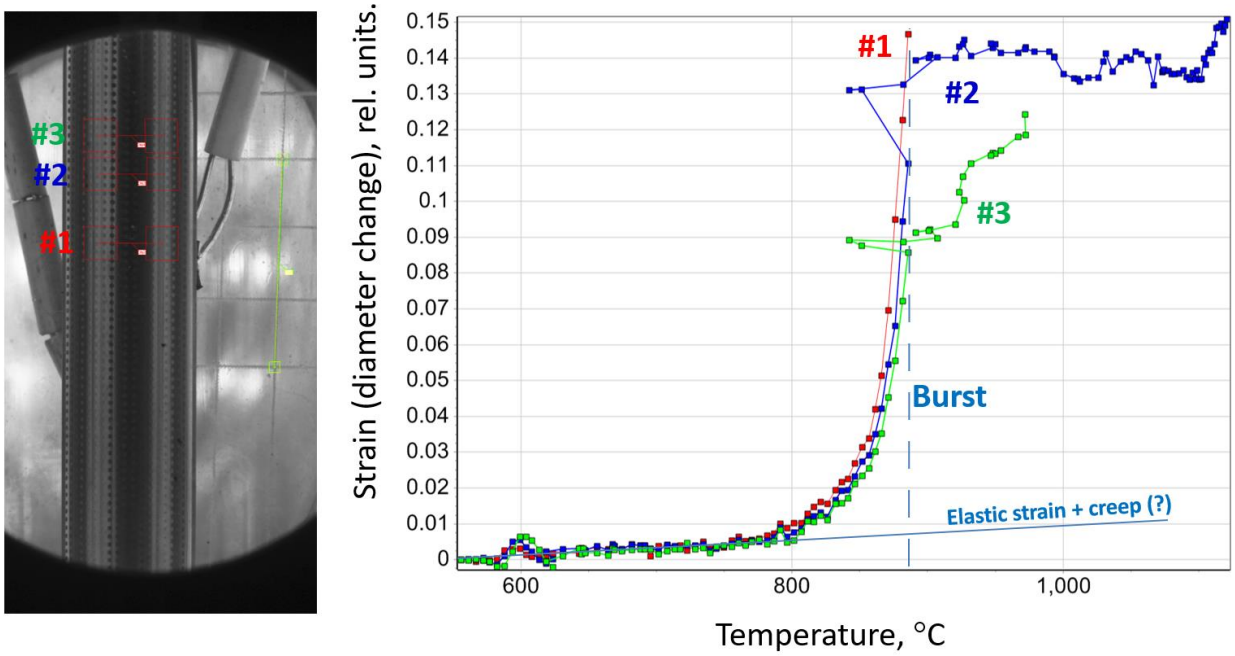

Figure 13. Hoop strain values as a function of temperature for a few selected locations on a FeCrAl alloy tube (left).

Figure 14 shows the dataset for another FeCrAl specimen. In this case, a much finer DIC pattern was engraved at the specimen surface using a laser engraver. To calculate strains, multiple DIC points (i.e., "nodes," over 100) were located along the red line. Note the strong brightness and contrast variations along the tube specimen diameter: light intensity varied strongly during the test, and heater reflections appeared at the specimen surface as the two bright bands, whereas the exact specimen top appeared to be dark. Conventional DIC gradient-based [11,12] algorithms were able to track the images; however, a number of iterations to get the solution was significantly larger compared to the constant-temperature DIC datasets (e.g., obtained during the common tensile test).

Nevertheless, the DIC data showed hoop strain along the tube specimen length (Figure 14). The graph represents unfiltered, nonsmoothed results for each DIC node; further data processing (e.g., smoothing) may improve the curve appearance and reveal additional details. The diagram demonstrates that the hoop strain reached a maximum near the specimen middle and decreased near the specimen ends. Strain

difference along the length appeared only when plastic deformation (i.e., ballooning) occurs (~750°C). Note the curves represent as-received, nonsmoothed data; some fluctuations are visible, reflecting the contribution of optic noise, air turbulence, and other factors. Further data processing (e.g., smoothing) will be beneficial.

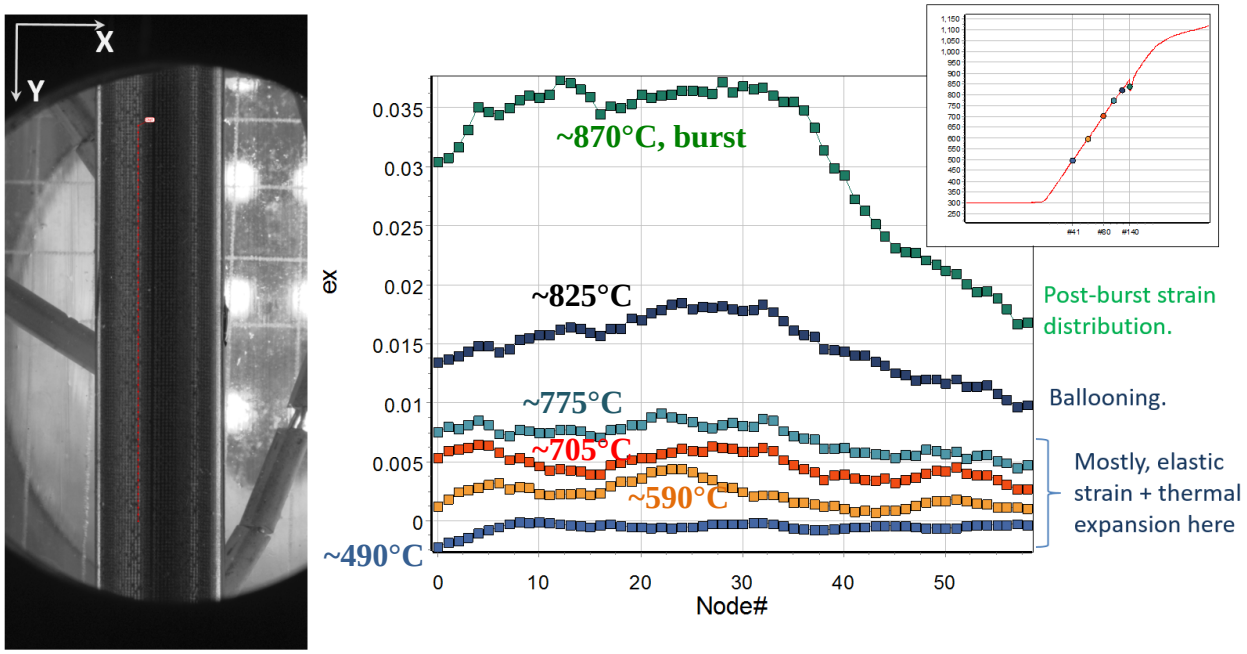

Figure 14. Strain distribution (hoop strain) along the specimen length at different temperatures on a FeCrAl alloy tube.

The results shown in Figure 13 and Figure 14 demonstrate the very high potential of DIC-assisted testing for evaluating and measuring strain distribution along the tube specimens. In addition to the hoop strains, DIC potentially allows for calculating strains along the axis and for getting shear strains if they appear during the test. At the same time, conventional DIC algorithms and software are difficult (and often impossible) to use with tube burst datasets because strong variations in the lighting conditions and changes in the surface quality (e.g., oxidation, interaction with steam) lead to tracking loss and unpredictable outcome. More robust computational approaches are necessary.

4. SUMMARY AND FUTURE WORK

In this project, an advanced tube burst test approach was offered and implemented. The approach includes a digital camera, optic system, and DIC algorithms as key components for getting in situ strain data for the tube specimen loaded by internal pressure and being heated at high heating rates (5°C/s). Several trial runs demonstrated the key advantages of this approach: (1) the temperature corresponding to the plastic strain initiation may be precisely defined, (2) hoop and axial strains may be measured as a function of temperature and internal pressure, and (3) strain distribution along the visible specimen axis may be calculated, if necessary.

This project identified several severe challenges and partially mitigated them; namely, image blurring and distortions caused by air convection were important factors limiting accuracy and precision. The project team tested mitigation strategies involving the proper design of the quartz tube. DIC patterns of acceptable quality were created using laser engraving; as expected, laser engraving had limited impact on the tube specimen's mechanical behavior and interaction with the steam. However, further work in this direction is necessary.

Although the DIC data could be processed, at least partly, using conventional DIC techniques (e.g., gradient-based Newton-Raphson algorithm family [11]), more reliable, stable, and robust methods are necessary. The cornerstones of common DIC are (1) stable surface pattern, (2) stable light conditions, and (3) optically stable environment. These principles may be compromised during tube burst test; thus, adaptation and customization of DIC algorithms are needed to get the best, cutting-edge results (e.g., tracking a changing object in a changing environment under variable lighting conditions).

Further modification of the technique may include testing longer-length specimens; this will require some furnace redesign (e.g., round optic ports [Figure 5], should be replaced with long narrow windows). Potentially, four projections of the tube specimen (360° view) may be recorded after furnace modification (if windows are present on all sides of the furnace). This step will require the careful calculation of the energy flow and distribution inside the furnace as well as heat losses (i.e., temperature field disturbance) caused by windows. Additionally, the thermal vision technique would be a good addition to in situ analysis.

The data collected during this project represents an initial baseline compilation. Optimization of the technique will allow for a multifaceted approach to benchmarking the burst behavior of zirconium as a function of numerous variables anticipated during burnup, such as waterside oxide layer formation and hydrogen pickup. Use of these datasets to benchmark the predictions of fuel performance codes such as BISON will increase confidence in their underlying assumptions and in turn allow for a similar approach to be taken for evolutions only possible when irradiation is introduced.

5. REFERENCES

[1] K.-T. Kim, "Evolutionary developments of advanced PWR nuclear fuels and cladding materials," *Nuclear Engineering and Design* 263 (2013): 59–69.

[2] D. Olander, "Nuclear fuels–present and future," *Journal of Nuclear Materials* 389 (2009): 1–22.

[3] K. A. Terrani, S. J. Zinkle, and L. L. Snead, "Advanced oxidation-resistant iron-based alloys for LWR fuel cladding," *Journal of Nuclear Materials* 448 (2014): 420–435.

[4] Y. Che, G. Pastore, J. Hales, and K. Shirvan, "Modeling of Cr2O3-doped UO2 as a near-term accident tolerant fuel for LWRs using the BISON code," *Nuclear Engineering and Design* 337 (2018): 271–278.

[5] M. Veshchunov and V. Shestak, "Modeling of Zr alloy burst cladding internal oxidation and secondary hydriding under LOCA conditions," *Journal of Nuclear Materials* 461 (2015): 129–142.

[6] R. Chapman, J. Crowley, A. Longest, and G. Hofmann, "Zirconium cladding deformation in a steam environment with transient heating," in *Zirconium in the Nuclear Industry: Proceedings of the Fourth International Conference* (Philadelphia: ASTM International, 1979). A. Terrani, "In-situ tube burst testing and high-temperature deformation behavior of candidate materials for accident tolerant fuel cladding," *Journal of Nuclear Materials* 466 (2015): 417–425.

[8] M. D. Novak and F. W. Zok, "High-temperature materials testing with full-field strain measurement: experimental design and practice," *Review of Scientific Instruments* 82 (2011): 115101.

[9] T. K. Sawarn, S. Banerjee, K. Pandit, and S. Anantharaman, "Study of clad ballooning and rupture behavior of fuel pins of Indian PHWR under simulated LOCA condition," *Nuclear Engineering and Design* 280 (2014): 501–510.

[10] X. Guo, J. Liang, Z. Tang, B. Cao, and M. Yu, "High-temperature digital image correlation method for full-field deformation measurement captured with filters at 2600 C using spraying to form speckle patterns," *Optical Engineering* 53 (2014): 063101.

[11] H. Bruck, S. McNeill, M. A. Sutton, and W. Peters, "Digital image correlation using Newton-Raphson method of partial differential correction," *Experimental Mechanics* 29 (1989): 261–267.

[12] H. Schreier, J.-J. Orteu, and M. A. Sutton, *Image Correlation for Shape, Motion and Deformation Measurements* (New York: Springer US, 2009).